This article has been accepted for publication in Journal of Lightwave Technology. This is the author's version which has not been fully edited and content may change prior to final publication. Citation information: DOI 10.1109/JLT.2026.3717366

Nonlinearity Compensation for Coherent Optical Satellite Communications

Stella Civelli, *Member, IEEE*, Luca Potì, *Senior Member, IEEE*, Enrico Forestieri, *Life Member, IEEE*, and Marco Secondini, *Senior Member, IEEE*

***Abstract*—Optical satellite uplinks rely on high-power optical amplifiers (HPOAs) to overcome free-space attenuation and enable long-distance transmission. However, at high power levels, fiber Kerr nonlinearity becomes significant and degrades system performance. In this work, we develop a realistic model for optical uplinks that accounts for nonlinear effects and analyze their impact, highlighting key differences from conventional long-haul fiber systems. We then introduce low-complexity digital signal processing techniques for nonlinearity compensation, based on constellation shaping via a look-up table (LUT) and a simple nonlinear phase rotation applied at the transmitter and/or receiver. The LUT also enables adaptive rate tuning according to channel conditions, enhancing robustness against link variations. Simulation results show that the proposed techniques increase the maximum acceptable link loss by up to 6 dB with negligible complexity. Finally, we show that, at the system level, propagation in the HPOA can be modeled as a simple nonlinear phase rotation, equivalent to propagation in a zero-dispersion noiseless fiber link, and fully characterized by a single parameter—the characteristic nonlinear power.**

***Index Terms*—Optical satellite communication, nonlinear optical channel, high power optical amplifiers.**

I. Introduction

RECENTLY, optical satellite communication has emerged as an effective technology to complement—and potentially replace—conventional radio-frequency satellite links [1]–[4]. Ground-to-satellite optical links, however, suffer from severe impairments caused by time-varying atmospheric conditions and by the relative motion between the satellite and the Earth (i.e., varying pointing angle), both leading to significant attenuation and performance degradation. To ensure sufficient received power at the satellite, thereby improving throughput and maintaining resilience under adverse conditions, the launch power should be as high as possible.

While free-space optical communications provide several advantages for satellite networks, the ground-to-satellite uplink remains a critical challenge [5]. Its performance is significantly affected by atmospheric phenomena such as scattering [1], molecular absorption [3], and turbulence [6]. Connectivity losses caused by cloud coverage can be mitigated through the use of optical ground station diversity [7], and adaptive optics techniques are commonly employed to reduce beam distortions induced by atmospheric turbulence [8]. However, even with these mitigation strategies, a fundamental asymmetry persists between the uplink and downlink power requirements. This asymmetry arises from the so-called shower curtain effect [9], [10], whereby the impact of a scattering layer depends on its position within the optical path. Since the ground station is located within the atmospheric scattering layer, the uplink is more severely degraded than the downlink, necessitating higher optical transmit power to compensate for atmospheric impairments. Consequently, scaling the optical power of ground station transmitters is a key requirement for achieving high data-rate satellite uplinks.

A typical architecture for uplink optical transmission is shown in Fig. 1, where a standard optical transmitter (TX) prepares the signal and feeds it into a high-power optical amplifier (HPOA), which is required to achieve the high optical power needed for the application. An optical fiber (OF), e.g., an output pigtail or a short optical patch cord, delivers the signal to the optical ground station (OGS), which is used for beam preparation and pointing. In this context, external-cavity lasers followed by fiber-based HPOAs represent a natural choice for OGS transmitters, owing to their capability to deliver high average power while maintaining excellent beam quality. Recently, several HPOAs have been demonstrated, including in-band core-pumped Er-doped fibers [11], cladding-pumped Er-doped fibers [12], and cladding-pumped ErYb co-doped fibers [13]. All these approaches exhibit physical and practical constraints or limitations, making custom designs necessary depending on the specific application [14]. Indeed, ongoing research explores more efficient architectures to improve pump-to-signal conversion and mitigate nonlinear effects, though challenges in efficiency, thermal stability, and space qualification remain [15].

Among the main challenges, fiber nonlinearities inevitably arise when high-power signals propagate through optical fibers—either within the doped fiber inside the amplifier or along the output pigtail and additional patch cords [16]. Their mitigation is essential to increase the launch power, thereby enabling higher throughput or longer transmission distances [17], [18]. On one hand, nonlinear effects can be mitigated through dedicated HPOA designs. For instance, erbium-doped fiber amplifiers (EDFAs) typically require longer doped fibers compared to erbium-ytterbium codoped amplifiers (EYDFAs), making the latter more attractive for reducing nonlinear impairments. However, very-high-power EYDFAs suffer from higher-order mode power transfer, leading to pointing instability, as well as long-term power degradation due to photo-

S. Civelli is with the Cnr-Istituto di Elettronica e di Ingegneria dell'Informazione e delle Telecomunicazioni (CNR-IEIIT), Pisa, Italy. S. Civelli, M. Secondini and E. Forestieri are with the Telecommunications, Computer Engineering, and Photonics (TeCIP) Institute, Scuola Superiore Sant'Anna, Pisa, Italy. M. Secondini, E. Forestieri and L. Potì with the National Laboratory of Photonic Networks, CNIT, Pisa, Italy. L. Potì is with the Universitas Mercatorum, Rome, Italy. Email: stella.civelli@cnr.it.

This article has been accepted for publication in Journal of Lightwave Technology. This is the author's version which has not been fully edited and content may change prior to final publication. Citation information: DOI 10.1109/JLT.2026.3717366

darkening [14]. Recently, an Er-based HPOA delivering up to 50 dBm was proposed specifically to mitigate nonlinear effects by combining a conventional EDFA stage with a large-mode-area EDFA stage [19]. However, large-mode-area solutions still face practical limitations, including the limited availability of reliable commercial components and the difficulty of maintaining stable single-mode operation.

On the other hand, fiber nonlinearity can also be mitigated through proper signal design and digital signal processing (DSP). For example, the Kerr nonlinearity arising in a short single-mode-fiber (SMF) pigtail following an HPOA was investigated in [18], where a compensation method for direct-detection systems was proposed. Furthermore, coherent optical communications are becoming increasingly relevant for space applications, enabling more advanced DSP techniques and higher throughput [2], [20].

In this context, the objective of this work is not to identify optimal amplifier designs or to provide a comprehensive overview of existing amplification architectures. Rather, the focus is on modeling nonlinear effects in coherent optical satellite communication uplinks and on developing low-complexity DSP-based mitigation strategies that can be applied independently of the specific amplification solution adopted, enabling higher launch powers and, consequently, longer transmission distances or higher data rates. The proposed approaches mainly rely on the mitigation of nonlinear phase rotation and the containment of spectral broadening through optimized probabilistic constellation shaping and pre- and post-compensation techniques. To validate the proposed model and assess the effectiveness of the considered techniques, three representative amplifier configurations, characterized by significantly different performance levels and inspired by both literature [12], [19] and commercial solutions [21], are analyzed as case studies. This work extends the results presented in [22] by providing a detailed channel model, a theoretical analysis of Kerr nonlinear effects in HPOAs, and a comprehensive numerical performance assessment under different compensation techniques and operating scenarios.

The paper is organized as follows. Section II presents a comprehensive system model and introduces a simplified model that accurately captures the system behavior. Section III proposes two DSP techniques for the compensation of nonlinearity: probabilistic constellation shaping and nonlinear phase compensation (NLPC). Both Sections II and III provide a comparison with long-haul fiber systems, whose nonlinear effects have been thoroughly investigated over the past decades. Section IV presents the system setup and a detailed numerical analysis of the system and the proposed DSP techniques under different conditions. Finally, Section V draws the conclusions.

II. System Model

We consider a coherent ground-to-satellite optical link, sketched in Fig. 1. Fig. 2 illustrates the equivalent complex baseband representation adopted throughout this work. The system comprises a ground-based transmitter, a short high-power optical fiber stage including amplification, a free-space optical (FSO) link toward the satellite, and a coherent receiver. In the following, each subsystem is described in detail.

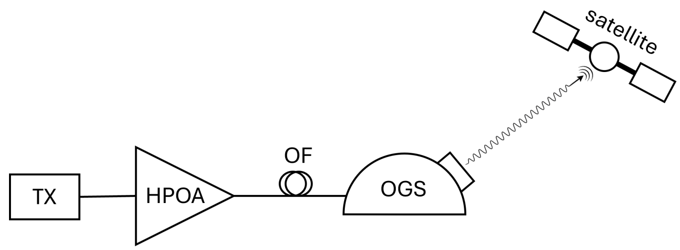

Figure 1. Ground-to-satellite optical link.

A. Transmitter

At the transmitter (TX), information bits are mapped by DSP onto a dual-polarization (DP) M-ary quadrature amplitude modulation (QAM) signal with baud rate R. The resulting complex baseband signal can be written as

$$\mathbf{x}(t) = \sum_k \mathbf{a}_k \, p(t - kT) \tag{1}$$

where $\mathbf{a}_k = [a_{k,x}, a_{k,y}]^{\mathrm{T}}$ contains the couple of complex QAM symbols transmitted on the two orthogonal polarizations, $p(t)$ is the pulse shape, and $T = 1/R$ the symbol time. Optional digital pre-distortion may be applied at this stage.

Each polarization component is decomposed into its in-phase and quadrature parts. Consequently, the DP signal is represented by four real-valued electrical waveforms (I/Q components for the two polarizations), which are converted into analog form by four digital-to-analog converters (DACs).

The resulting analog signals are applied to a dual-polarization IQ modulator, which maps them onto the two orthogonal polarization states of a continuous-wave optical carrier generated by a narrow-linewidth laser source. Under the complex baseband representation adopted in this work, the combined effect of DACs, drivers, and modulator bandwidth limitations is captured by $H_{\mathrm{TX}}(f)$.

The resulting optical signal is subsequently amplified by an HPOA and delivered to the OGS output through a short fiber section (patch cord or pigtail).

B. Optical Fiber Channel

The optical signal propagates through two short fiber sections: the active fiber inside the HPOA and the passive delivery fiber (patch cord). Although their total length is typically below 100 m, the launched optical power may exceed 35–40 dBm, making nonlinear effects significant.

Propagation of the dual-polarization signal in both sections is described by the Manakov equation for the complex en-

This article has been accepted for publication in Journal of Lightwave Technology. This is the author's version which has not been fully edited and content may change prior to final publication. Citation information: DOI 10.1109/JLT.2026.3717366

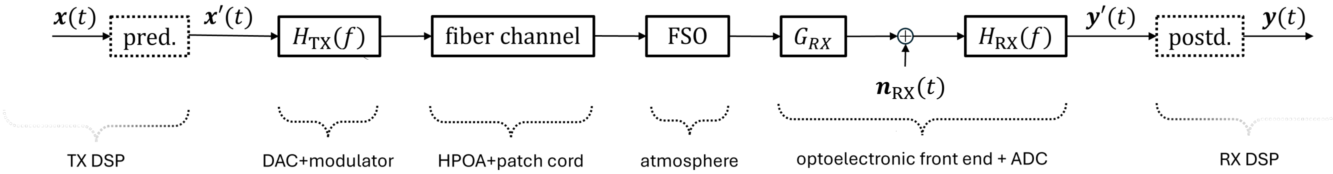

Figure 2. Equivalent baseband model of the coherent optical uplink system, including hardware and channel impairments. Dashed blocks denote optional DSP compensation functions at the TX and RX.

velope $\mathbf{u}(z,t) = [u_x(z,t), u_y(z,t)]^T$, normalized such that $E\{\|\mathbf{u}(z,t)\|^2\} = 1$ [23][1]

$$\frac{\partial \mathbf{u}}{\partial z} = j\frac{\beta_2}{2}\frac{\partial^2 \mathbf{u}}{\partial t^2} - j\gamma P g(z)\|\mathbf{u}\|^2\mathbf{u} + \mathbf{n}_{\mathrm{ASE}} \tag{2}$$

where P is the output optical power (on both polarizations), γ is the Kerr nonlinear coefficient, β_2 is the group-velocity dispersion, $g(z)$ is the normalized longitudinal power profile ($g(L) = 1$, with L the total fiber length) accounting for both gain and loss, and $\mathbf{n}_{\mathrm{ASE}}(z,t)$ is the amplified spontaneous emission (ASE) noise. Below, the dominant physical effects are discussed.

1) Amplification and Noise: The HPOA is modeled as a distributed-gain active fiber generating ASE along the propagation coordinate z. The longitudinal power profile $g(z)$ and the power spectral density (PSD) of the ASE noise term $\mathbf{n}_{\mathrm{ASE}}(z,t)$ are obtained from the standard coupled propagation and population equations governing doped-fiber amplifiers, evaluated under the assumption of a continuous-wave input signal, flat gain and ASE spectra over the signal bandwidth. Under these assumptions, the computed gain and noise profiles are treated as known quantities and incorporated into the normalized Manakov equation (2) to assess their impact on signal propagation. By contrast, the patch cord is a passive fiber, where $g(z)$ is determined only by fiber attenuation and no ASE noise is generated ($\mathbf{n}_{\mathrm{ASE}}(z,t) = 0$).

As will be shown later, although gain and ASE are generated continuously along the HPOA, their detailed longitudinal distribution is irrelevant from a system-level perspective, since only the output quantities determine performance. To characterize them, we introduce two lumped parameters. The first is the amplifier gain $G_{\mathrm{HPOA}} = P/P_{\mathrm{IN}}$, defined as the ratio between output and input signal power. The second is the noise figure F_{HPOA}, which quantifies the degradation of the signal-to-noise ratio (SNR) introduced by the amplifier and therefore determines the PSD of the ASE noise accumulated at the HPOA output, $N_{\mathrm{HPOA}} = G_{\mathrm{HPOA}}F_{\mathrm{HPOA}}h\nu/2$ (per polarization).

2) Chromatic Dispersion: The first term of the right-hand side of (2) is responsible for chromatic dispersion, which induces a temporal broadening of the propagating optical pulses. For a pulse of width T_0, the amount of broadening increases with the ratio L/L_D, where

$$L_D \triangleq \frac{T_0^2}{|\beta_2|} \tag{3}$$

is the dispersion length [24, eq (3.1.5)]. We can readily verify that in the typical scenario considered in this work, $L \ll L_D$, indicating a negligible broadening of the propagating signal. For instance, for a 100 GBd signal in a standard SMF, assuming $\beta_2 = -21.7\,\mathrm{ps}^2/\mathrm{km}$ and $T_0 \approx T = 10\,\mathrm{ps}$, $L_D \approx 4.6\,\mathrm{km}$, whereas the total fiber length L is typically below 100 m.

3) Kerr Nonlinearity: In contrast, Kerr nonlinearity—the second term on the right-hand side of (2)—plays a central role due to the high optical power. When $L \ll L_D$, chromatic dispersion can be neglected and, in the absence of ASE noise, propagation is dominated by the Kerr nonlinear term. In this case, (2) can be solved in closed form as

$$\mathbf{u}(L,t) = \mathbf{u}(0,t)\exp\left(-j\bar{\phi}\|\mathbf{u}(0,t)\|^2\right) \tag{4}$$

with

$$\bar{\phi} = P\int_0^L \gamma g(z)dz \tag{5}$$

According to (4), the optical signal undergoes a phase rotation proportional to its instantaneous power, a phenomenon known as *self-phase modulation* (SPM). The strength of SPM depends on the dimensionless parameter $\bar{\phi}$ in (5), which represents the average accumulated nonlinear phase rotation (NLPR). For convenience, we rewrite it as $\bar{\phi} = P/P_{\mathrm{NL}}$, where we have introduced the characteristic nonlinear power

$$P_{\mathrm{NL}} = \left(\int_0^L \gamma g(z)dz\right)^{-1} \tag{6}$$

representing the power scale at which SPM becomes significant. For instance, the EDFA considered in Section IV-A (Setup A) yields $P_{\mathrm{NL}} \approx 42.7\,\mathrm{dBm}$.

We distinguish three main effects associated with SPM.

a) Nonlinear phase rotation (NLPR): Each received symbol undergoes a different power-dependent phase rotation. In the absence of chromatic dispersion, symbols do not spread nor interact through linear memory, and therefore the nonlinear distortion remains temporally uncorrelated. In principle, NLPR is a deterministic effect which can be exactly compensated by applying the inverse phase rotation at either the transmitter or the receiver, as discussed in Section III-B. In practice, however, compensation is fundamentally limited by the additional effects described below. Moreover, unlike long-haul

[1] The small random birefringence unavoidably present in optical fibers gives rise to an additional polarization-dependent nonlinear term. In standard telecom fibers, the birefringence correlation length is typically much shorter than the propagation distance. As a result, the contribution of this term averages out along the link and is generally negligible at the system level. Its possible relevance in the scenario considered here is left for future investigation. Other nonlinear mechanism (e.g., Raman, Brillouin, ...) are not included in the model, since Kerr effect is expected to be the dominant impairment [18].

This article has been accepted for publication in Journal of Lightwave Technology. This is the author's version which has not been fully edited and content may change prior to final publication. Citation information: DOI 10.1109/JLT.2026.3717366

dispersive links, the absence of temporal correlation in the NLPR prevents its mitigation through conventional carrier phase recovery algorithms that rely on temporal averaging [25].

b) Spectral broadening: SPM inherently implies spectral broadening, since the phase shift in (4) induces a time-varying frequency chirp that depends on the derivative of the signal intensity. In conventional systems operating on standard SMF fibers in the C band, spectral broadening is strongly suppressed by chromatic dispersion and is therefore typically negligible. By contrast, in the present scenario, where $L \ll L_D$, it may become significant and, combined with the finite bandwidth of practical TXs and RXs, degrade system performance and limit the effectiveness of NLPR compensation.

In this dispersionless regime, under the assumption of independent and statistically equivalent polarizations with circularly symmetric complex Gaussian statistics, the evolution of the PSD can be derived analytically. Letting

$$R(z,\tau) \triangleq E\{u_x(z,t+\tau)u_x^*(z,t)\} = E\{u_y(z,t+\tau)u_y^*(z,t)\} \tag{7}$$

denote the autocorrelation function of each polarization component of the normalized envelope at distance z, one obtains (see Appendix)

$$R(L,\tau) = \frac{R(0,\tau)}{\left[1+\bar{\phi}_{\mathrm{NL}}^2(1/4-|R(0,\tau)|^2)\right]^3} \tag{8}$$

The PSD follows from the Wiener–Khinchin theorem as

$$S(z,f) = \int_{-\infty}^{\infty} R(z,\tau)e^{-j2\pi f\tau}d\tau. \tag{9}$$

The accuracy of this analytical expression will be verified in Section IV-B.

c) Signal–noise interaction: During propagation inside the HPOA, ASE noise is continuously generated, as described by the distributed noise term in (2). In principle, this ASE component co-propagates with the signal and causes random intensity fluctuations that, through (4), are converted to random phase fluctuations (nonlinear phase noise).

In the considered scenario, however, the amount of ASE generated within the amplifier is typically negligible compared to other sources of noise in the system. As a consequence, the corresponding nonlinear signal–noise interaction is also negligible, and the overall SNR is essentially determined by the receiver noise.

On the other hand, receiver noise, although it does not physically interact with the signal inside the nonlinear fiber, may give rise to an indirect but analogous form of signal–noise interaction when attempting to invert (4) by DSP at the receiver. This mechanism, which will be analyzed in the following, ultimately limits the practical mitigation of NLPR.

C. Free-Space Optical Channel

After leaving the OGS, the optical signal propagates through an FSO link toward the satellite.

All time-varying propagation effects—such as atmospheric turbulence, scattering, and molecular absorption—are treated in a static manner. The wireless channel is therefore simply modeled as a constant attenuation factor $\mathcal{L}$, representing the overall link loss between ground and satellite.

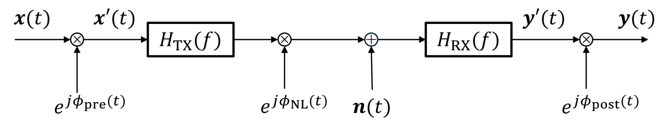

Figure 3. Simplified equivalent baseband model derived from Fig. 2 under the approximations in Section II-E, used for theoretical analysis and as a guideline for the development of the proposed DSP compensation techniques.

D. Receiver

At the receiver (RX), a preamplified coherent optoelectronic front-end is considered, comprising an optical preamplifier with gain G_{RX} and noise figure F_{RX}; a polarization- and phase-diversity coherent receiver with balanced photodetectors; and four analog-to-digital converters (ADCs), one per each quadrature component of each polarization. The optical pre-amplifier introduces an additive white Gaussian noise (AWGN) contribution $\mathbf{n}_{\mathrm{RX}}(t)$ with PSD $N_{\mathrm{RX}} = G_{\mathrm{RX}}F_{\mathrm{RX}}h\nu/2$ per polarization. The receiver is assumed ideal, except for the finite electrical bandwidth of the photodetectors and ADCs, by the low-pass transfer function $H_{\mathrm{RX}}(f)$.

The digitized samples are finally processed by DSP, which includes optional NLPR compensation, matched filtering, and symbol-rate sampling. More details about DSP are provided in Section III and IV-A.

E. Simplified Model

Based on the above considerations, the baseband model in Fig. 2 can be simplified as in Fig. 3, where the fiber channel is simply modelled by the NLPR $\phi_{\mathrm{NL}}(t) = -\bar{\phi}\|\mathbf{u}(0,t)\|^2$ in (4) (neglecting dispersion and signal–noise interaction), and the AWGN term $\mathbf{n}(t) = [n_x(t), n_y(t)]^T$ accounts for the contribution of all noise sources and for the effect of gains and losses, with an overall SNR (per symbol)

$$\mathrm{SNR} = \frac{P}{R_s h\nu(\mathcal{L}F_{\mathrm{RX}} + G_{\mathrm{HPOA}}F_{\mathrm{HPOA}})} \approx \frac{P}{R_s h\nu\mathcal{L}F_{\mathrm{RX}}} \tag{10}$$

The approximation in (10) holds when $\mathcal{L} \gg G_{\mathrm{HPOA}}$, i.e., in the practically relevant scenario of strong channel loss.

This simplified model captures the most relevant characteristics of the channel, namely, AWGN, bandwidth constraints, NLPR, and the associated spectral broadening. It will therefore be used in the following to design and optimize the system and to provide a theoretical interpretation of the results.

In particular, based on this model, we restrict transmitter predistortion and receiver post-compensation to simple phase rotations—$\phi_{\mathrm{pre}}(t)$ and $\phi_{\mathrm{post}}(t)$, respectively—as detailed in Section III-B.

On the other hand, simulation results will be obtained using the more accurate physical model described previously. Nevertheless, we will demonstrate that the simplified model reproduces them with good accuracy and can, in principle, replace the full physical model even for reliable performance estimation.

This article has been accepted for publication in Journal of Lightwave Technology. This is the author's version which has not been fully edited and content may change prior to final publication. Citation information: DOI 10.1109/JLT.2026.3717366

III. Digital Techniques for Nonlinearity Compensation

In this section, we discuss and analyze DSP techniques for the mitigation of the HPOA nonlinearity. The proposed techniques are inherited from optical fiber communication and tailored to the HPOA scenario.

A. Probabilistic Constellation Shaping

Probabilistic constellation shaping has been known for several decades, and nowadays is commonly adopted in optical fiber coherent systems with the dual objective of improving system performance and enabling fine-tuning of the transmission rate. Probabilistic shaping is commonly implemented through the probabilistic amplitude shaping (PAS) architecture, in which a distribution matcher (DM) maps information bits onto amplitudes with the desired probability distribution, while the signs remain uniformly distributed and are used for forward error correction (FEC) [26]. The main component of PAS is the DM, which maps k information bits onto N shaped amplitudes (where N denotes the block length) drawn from the M-ary alphabet $\{1, 3, \ldots, 2M-1\}$, achieving a DM rate $R_{\mathrm{DM}} = k/N$. The N amplitudes are then combined with N signs (with uniform distribution), to form $N/4$ couples of complex QAM symbols modulating the signal in (1).[2] The accuracy of the DM depends on the specific implementation but typically improves when N increases [25], [27], [28]. In general, algorithmic DMs, such as constant-composition DM (CCDM), enumerative sphere shaping (ESS), and their variants, achieve good performance at the cost of non-negligible complexity for large N [27], [28]. By contrast hierarchical DMs based on look-up-tables (LUTs) have negligible complexity but reduced performance [29], [30]. When N is very small, the DM can be implemented efficiently with a single LUT, simply storing the 2^k best sequences of N amplitudes. In the linear regime with an average power constraint, the optimal DM scheme is denoted as sphere shaping (SpSh), corresponding to mapping information on sequences with minimum energy. An example of LUT-based SpSh encoding is shown in Fig. 4 for $k = 5$, $N = 4$, and $M = 4$, ($R_{\mathrm{DM}} = 1.25$ bits/amplitude, 64QAM constellation). The k input bits determine the LUT address containing the output amplitude sequence. Correspondingly, the decoding LUT has M^N entries—one for each possible sequence of N amplitudes—each returning the associated k bits.[3] Overall, the memory required for the encoding and decoding LUTs is $2^k N \log_2 M$ and $M^N k$ bits, respectively.

PAS provides two main advantages, discussed below: shaping gain and rate adaptability. Thanks to these features, PAS has also been proposed for free-space optical communications [20].

Rate adaptability refers to the ability to vary the information rate (IR) for a fixed FEC code rate c and constellation order, by solely adjusting the DM rate. Specifically, the information rate is given by $\mathrm{IR} = R_{\mathrm{DM}} + 1 - (1-c)m$ in bits per 1D symbol, where $m = \log_2 M + 1$ is the number of bits per 1D symbol [31]. This property is particularly attractive for satellite communications, where channel conditions can vary significantly, for instance due to cloud coverage. When using a LUT with block length N, the rate can be adapted by simply decreasing k—i.e., using only the first 2^k entries of the LUT—in steps of $1/N$, with finer granularity for larger N.

Shaping gain refers to the improved performance compared to uniform constellations. In the linear regime, PAS aims at reducing the mean energy per symbol for a fixed IR, and approaches Shannon capacity as N increases, providing up to 1.53 dB gain over an AWGN channel compared to the uniform constellation by targeting the Maxwell–Boltzmann (MB) distribution, a sort of *discretized* Gaussian distribution [26].

PAS has also been investigated for mitigating nonlinearities in optical fiber communication, but with limited gains [25], [28], [32]. Here the mechanism relies on the correlations induced by the DM among the amplitudes within each block, which reduce the nonlinear interference generated during propagation. This effect is more pronounced for shorter block lengths N. As a result, the overall shaping gain is maximized for a block length that balances linear and nonlinear effects and depends on the channel memory, i.e., on the accumulated dispersion. The optimal N is generally very long (N>100) for multi-span fiber links (in C-band with SMF), and shorter ($N \sim 30$) for single-span links, but in any case too long for a single-LUT implementation. Moreover, the long memory of these fiber channels implies that carrier phase recovery algorithms that are commonly employed to address laser phase noise are also capable of mitigating the generated nonlinear interference, hiding the nonlinear shaping gain in most cases [25], [33].

The picture is quite different for satellite optical coherent up-links with HPOAs. While the behavior in the linear regime remains unchanged, the nonlinear regime differs due to the nearly dispersionless nature of the fiber channel, which makes nonlinearity an almost instantaneous (memoryless) effect, as discussed in Section II. This leads to two key consequences, which will be quantified and analyzed in Section IV-C: i) the optimal PAS block length N becomes much shorter, making a single-LUT implementation of the DM—such as the one depicted in Fig. 4—particularly attractive; ii) carrier phase recovery algorithms are ineffective in mitigating nonlinear interference, increasing the relevance of the nonlinear shaping gain provided by PAS.

B. Nonlinear Phase Compensation (NLPC)

Assuming the simplified model in Fig. 3, fiber propagation reduces to the phase rotation in (4), which can be inverted at the TX or RX DSP by applying the inverse rotation. We refer to this operation as *nonlinear phase compensation* (NLPC). In the absence of bandwidth limitations and noise, exact inversion could be equivalently performed at the TX or RX. In practice, however, bandwidth limitations and noise prevent exact inversion, as discussed below.

[2] Different mapping strategies are possible—e.g., mapping the DM amplitudes independently on each quadrature component of each polarization [25]—but are not considered in this work.

[3] Since not all M^N amplitude sequences are actually needed, a more efficient implementation of the decoding LUT may be devised.

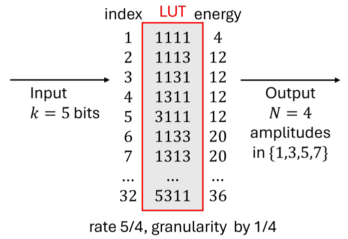

Figure 4. LUT with $N = 4$ amplitudes from $\{1, 3, 5, 7\}$ and 32 entries ($k = 5$), corresponding to a 64QAM SpSh constellation with rate 4.5 bits/2D.

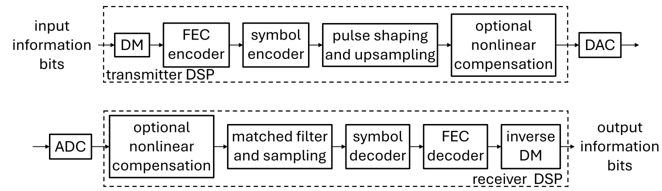

Figure 5. Transmitter and receiver DSP.

At the RX, the transfer function $H_{\mathrm{RX}}(f)$ filters out part of the spectrally broadened signal, preventing exact inversion of (4). Similarly, at the TX, accurate pre-compensation would require generating frequency components that may lie outside the available bandwidth defined by $H_{\mathrm{TX}}(f)$. To mitigate the effect of bandwidth limitations, it would be advantageous to split the NLPC equally between TX and RX, minimizing the maximum spectral broadening experienced by the signal at both locations. However, the noise injected between the HPOA and the RX breaks the symmetry between TX and RX processing, degrading only the effectiveness of RX-side NLPC. Furthermore, complexity and power consumption constraints are also asymmetric between satellite and ground terminals, generally favoring TX processing.

For these reasons, we consider a split NLPC between TX and RX, with splitting ratio κ

$$\mathbf{x}'[k] = \mathbf{x}[k]\exp(j\kappa\bar{\phi}\|\mathbf{x}[k]\|^2) \tag{11}$$

$$\mathbf{y}[k] = \mathbf{y}'[k]\exp(j(1-\kappa)\bar{\phi}\|\mathbf{y}'[k]\|^2) \tag{12}$$

where $\mathbf{x}[k]$, $\mathbf{x}'[k]$, $\mathbf{y}'[k]$, and $\mathbf{y}[k]$ denote the transmitted signal (before and after NLPC) and the received signal (before and after NLPC), respectively, as shown in Fig. 2 and 3, sampled at n samples per symbol. Based on the above discussion, the splitting ratio κ can be either optimized to maximize performance or set to $\kappa = 1$, corresponding to NLPC entirely performed at the TX. Both cases are analyzed in Section IV-C.

The complexity of NLPC, at the TX or RX side, measured as number of real multiplications (RM) per 2D symbols, is

$$C_{\mathrm{NLC}} = 5.5n \text{ RM/2D} \tag{13}$$

assuming that each complex multiplication is implemented with 3 real multiplications [34].

IV. Numerical Results

A. System Setup

System performance is evaluated through numerical simulations. A detailed system model is provided in Section II, while the transmitter and receiver DSP chains—operating with n samples/symbol—are shown in Fig. 5 and described below.

The TX-DSP, located at the ground station, maps information bits on symbols $\mathbf{a}_k$ in (1) drawn from a DP QAM constellation with uniform or probabilistically shaped distribution. In the latter case, the system uses the PAS approach, which combines DM and FEC in reverse concatenation order (the latter not included in our simulations) [26]. Unless otherwise stated, the pulse shape $p(t)$ in (1) has a root-raised cosine spectrum with roll-off 0.05, and the symbol rate is $R = 100$ GBd. An optional NLPC stage, defined in (11) and implemented with oversampling factor n, may be applied to (1) to obtain the signal $\mathbf{x}'(t)$.

Three different optical amplification configurations are considered:

- Setup A: an EDFA with 33 m of Er-doped fiber (dispersion $\beta_2 = -21.7\,\mathrm{ps}^2/\mathrm{km}$, nonlinear coefficient $\gamma = 3.6\,\mathrm{W}^{-1}\mathrm{km}^{-1}$), resulting in an overall characteristic nonlinear power $P_{\mathrm{NL}} \approx 42.68\,\mathrm{dBm}$;
- Setup B: the 100 W HPOA reported in [12], consisting of 40 m of large-mode-area Er-doped fiber ($\beta_2 = -21.7\,\mathrm{ps}^2/\mathrm{km}$, $\gamma = 0.2\,\mathrm{W}^{-1}\mathrm{km}^{-1}$), followed by 3 m of standard SMF ($\beta_2 = -21.7\,\mathrm{ps}^2/\mathrm{km}$, $\gamma = 1.27\,\mathrm{W}^{-1}\mathrm{km}^{-1}$) used as pigtails and patch cords, yielding $P_{\mathrm{NL}} = 51.24\,\mathrm{dBm}$;
- Setup C: the master-oscillator power-amplifier scheme described in [13], capable of delivering a record output power of 302 W, where the power amplifier consists of 6 m of Er/Yb co-doped large-mode-area fiber ($\beta_2 = -21.7\,\mathrm{ps}^2/\mathrm{km}$, $\gamma = 1.27\,\mathrm{W}^{-1}\mathrm{km}^{-1}$). To emulate a non-co-located optical transmitter and telescope architecture, an additional 20 m of passive fiber, with propagation characteristics identical to those of the active fiber, is included at the amplifier output to represent pigtails and interconnecting patch cords, resulting in an overall $P_{\mathrm{NL}} = 53.37\,\mathrm{dBm}$.

Unless otherwise specified, the results presented in the following are based on Setup A. A comparison with Setups B and C, which exhibit improved performance, as well as a validation of the simplified model across all three configurations, is provided in the final part of the paper. Fiber propagation according to (2) is evaluated numerically using the split-step Fourier method (SSFM) with a sufficiently large number of steps, including dispersion, nonlinear Kerr effects, gain, and distributed noise due to ASE.

After the HPOA, the signal is launched into free space and received at the satellite station. Propagation through the FSO channel is simply modeled as a lumped attenuation $\mathcal{L}$. The noise figure of the RX-side EDFA is $F_{\mathrm{RX}} = 4\,\mathrm{dB}$. The limited bandwidth of both TX- and RX-side opto-electronics components (DAC, ADC, modulator and photoreceiver) is accounted for by ideal rectangular filters $H_{\mathrm{TX}}(f) = H_{\mathrm{RX}}(f)$ with lowpass bandwidth $B = 55\,\mathrm{GHz}$. The overall signal bandwidth, including the pulse-shaping roll-off, is $1.05 \cdot R = 52.5\,\mathrm{GHz}$, leaving a small margin (about 5%) for spectral broadening. At the RX-DSP, an optional NLPC—defined in (12) and implemented with oversampling factor n as at the TX-side—can be applied, followed by matched filter and sampling at symbol time $1/R$. The resulting samples—a noisy version of the transmitted symbols—are compared with the transmitted symbols to evaluate the generalized mutual information (GMI), which quantifies the achievable information rate with ideal FEC and bit-wise decoding [35], [36]. In our simulations, the inverse DM and FEC decoding shown in Fig. 5 are not applied, since they are not required to compute the GMI. The TX and LO lasers are assumed ideal (zero linewidth), as the phase noise of typical telecom lasers at these baud rates can be effectively compensated by standard carrier phase recovery algorithms without performance penalty [37]. For a given launch power P, the performance is measured in terms of *acceptable link loss*, which is the maximum loss $\mathcal{L}$ for which a desired GMI can be achieved. Our metric is analogous to the power budget—typically defined as the maximum allowable loss for a desired pre-FEC bit error rate (BER)—but replaces the pre-FEC BER threshold with a target GMI. Achieving the target GMI (measured in bits/2D) ensures that, with an ideal FEC, the system can operate with arbitrarily low error probability at the corresponding bit rate $R_b = 2R \cdot \mathrm{GMI}$, where the factor 2 accounts for the two polarizations.[4] In our setup, unless otherwise stated, we consider two cases: (i) a target GMI of 3 bits/2D (corresponding to an achievable bit rate $R_b = 600\,\mathrm{Gb/s}$) on the shaped 64QAM constellation with shaping rate 4.5 bits/2D or with uniform (U)-16QAM or 64QAM; and (ii) target GMI of 5 bits/2D (corresponding to $R_b = 1\,\mathrm{Tb/s}$) on the 256QAM constellation with shaping rate 6.5 bits/2D or U-64QAM; the shaping rate has been optimized offline. Clearly, the acceptable link loss depends on the launched power P. It increases linearly with P until fiber nonlinearity remains negligible ($P \ll P_{\mathrm{NL}}$), then reaches a peak at the optimal power and decreases afterwards due to the NLPR and spectral broadening induced by the nonlinearity. Accordingly, we define the *maximum acceptable link loss* as the peak value achieved at this optimal launch power.

B. Spectral Broadening

Fig. 6 illustrates the spectral-broadening effect occurring in the HPOA (Setup A) for three different NLPC configurations: (a) without NLPC, (b) with TX-side NLPC, and (c) with NLPC evenly split between TX and RX. For each configuration, the left panel shows the PSD of the transmitted signal before the HPOA, while the right panel shows the PSD of the received signal after the HPOA. In these examples, the transmit and receive filters $H_{\mathrm{TX}}(f)$ and $H_{\mathrm{RX}}(f)$ are omitted so that the full extent of the spectral broadening can be observed, while their bandwidths are indicated by black dashed lines for reference. Numerical simulations based on the split-step Fourier method (SSFM), averaged over many realizations, are compared with the analytical prediction based on (8). The results are obtained for probabilistically shaped 64QAM signals at a launch power of $P = 43\,\mathrm{dBm}$ (corresponding to $\bar{\phi} \approx 1.1$). Probabilistic shaping is implemented either through i.i.d. symbols with an MB distribution, representative of ideal AWGN-optimal shaping and practically achievable for large block lengths N, or through SpSh with block length $N = 4$, corresponding to the simple LUT implementation shown in Fig. 4.

[4]For a specific realistic FEC, the target GMI can be replaced by the normalized GMI threshold evaluated for that FEC scheme [38].

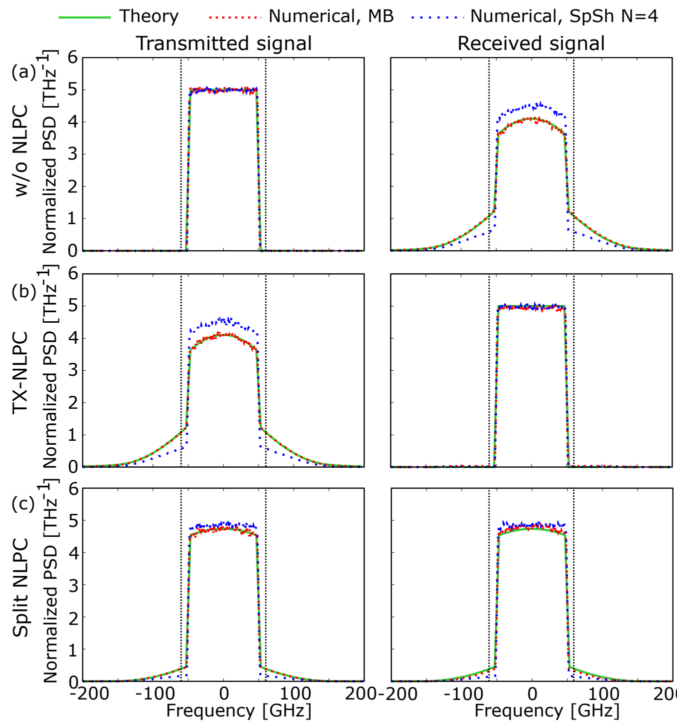

Figure 6. PSD of the normalized transmitted (left) and received (right) signals (100 GBd, $\bar{\phi} \approx 1.1$) obtained analytically from (8) or with numerical simulations (MB or SpSh with $N = 4$): (a) without NLPC; (b) with TX-side NLPC; and (c) with split NLPC.

Without NLPC (Fig. 6(a)), the PSD of the transmitted signal is solely determined by the pulse shape $p(t)$, independently of the adopted shaping scheme, and remains fully contained within the TX bandwidth. After propagation through the HPOA, however, significant spectral broadening occurs, causing part of the signal spectrum to extend beyond the available RX bandwidth and reducing the in-band PSD. In this condition, RX-side NLPC can mitigate, but not fully compensate, NLPR, since the out-of-band spectral components are irreversibly lost after detection. For i.i.d. MB symbols, the spectral broadening is more pronounced and closely follows the analytical prediction of (8). By contrast, SpSh with $N = 4$ exhibits reduced spectral broadening due to the strong correlation among the amplitudes of the four quadrature components within each DP symbol, an effect not captured by the analytical model. This observation suggests that reducing the PAS block length may help mitigate spectral broadening, although such behavior is not described by the simplified analytical expression in (8), which assumes i.i.d. symbols.

With TX-side NLPC (Fig. 6(b)), spectral broadening could be virtually removed from the RX signal, but at the expense of inducing a comparable broadening on the TX signal. Therefore, under symmetric TX and RX bandwidth constraints, TX-side and RX-side NLPC are expected to experience similar

This article has been accepted for publication in Journal of Lightwave Technology. This is the author's version which has not been fully edited and content may change prior to final publication. Citation information: DOI 10.1109/JLT.2026.3717366

bandwidth limitations and provide comparable performance. In this scenario, the impact of spectral broadening could be reduced by evenly splitting NLPC between TX and RX, as illustrated in Fig. 6(c).

C. System Performance

First, we analyze system performance for different modulation formats with uniform or shaped distributions. Fig. 7 shows the acceptable link loss versus launch power P for a target GMI of 3 bits/2D without NLPC, comparing U-16QAM, U-64QAM, i.i.d. symbols with MB distribution (an ideal benchmark distribution that is nearly optimal in the linear regime), and SpSh with very short ($N = 4$) and very long ($N = 256$) block lengths [28]. In all cases, PAS is implemented using 4D serial mapping: the N amplitudes generated by the same DM instance are mapped sequentially onto the quadratures and polarization components of the transmitted symbols. As a result, each DM instance generates $N/4$ 4D symbols, meaning that a DM with block length $N = 4$ generates a single 4D symbol [25], [39]. The figure shows that (i) in the linear regime, ideal MB shaping achieves the best performance, closely approached by SpSh with $N = 256$; (ii) performance drops in the nonlinear regime due to HPOA-induced nonlinearity; and (iii) in the nonlinear regime, ideal MB shaping performs worse than uniform constellations, while SpSh with a very short block length provides the best performance despite its large rate loss in the linear regime. This behavior arises from a trade-off between linear shaping gain and robustness to nonlinear effects for the different formats. For a given average symbol energy, the linear shaping gain increases with the constellation entropy, reaching its maximum with MB shaping, whereas nonlinear effects grow with the energy variations among the constellation symbols—being absent in a 4D constant-energy constellation, lower for uniform constellations, and largest for MB. SpSh with $N = 256$ closely approximates MB shaping, while SpSh with $N = 4$ provides the best trade-off between linear gain and nonlinear robustness. The advantage of SpSh with $N = 4$ is also evident in Figs. 6(a-c), which show its reduced spectral broadening compared to MB shaping.

A deeper analysis of the behavior of different shaping strategies is reported in Fig. 8, which shows the maximum acceptable link loss (at optimal power, taken at 1dB steps) for different DM block lengths N for a target GMI of 3 bits/2D and without NLPC. The figure compares the performance of ideal i.i.d. symbols with MB distribution, SpSh, shell mapping [25], constant composition distribution matcher (CCDM) [27], and one example of hierarchical DM (HiDM) [29], [30].[5] The figure shows that all techniques converge to the MB performance for long block lengths, with SpSh outperforming shell mapping, which in turn outperforms CCDM. This behavior, also observed in conventional fiber systems, is due to the rate loss of the considered DMs, largest for CCDM and smallest for SpSh. By contrast, in this scenario, the optimal block length for SpSh and shell mapping is much shorter ($N = 4$) than in conventional fiber systems [25], [40], [41], highlighting the importance of correlations between the four quadratures of a single 4D symbol rather than among adjacent symbols. Conversely, CCDM achieves its best performance with very long block lengths, due to the high rate loss incurred at short block lengths. The optimal SpSh with $N = 4$ can be implemented with a LUT with 32 entries, sketched in Fig. 4, containing the sequences of $N = 4$ amplitudes with lowest energy. Finally, HiDM (also implemented with LUTs) provides a good nonlinear performance, obtained with a longer block length $N = 64$, which may provide advantages in terms of rate granularity (by steps of $1/N$) and linear performance. Further optimization of HiDM may provide larger gains. In the following, unless otherwise stated, SpSh with block length $N = 4$ is considered as a shaping scheme and is simply referred to as NL shaping.

Next, we study the performance of the proposed NLPC technique, investigating its dependence on the splitting ratio

[5]The HiDM structure is made of 3 layers, with output amplitudes $[4, 4, 4]$, input bits $[1, 13, 12]$ and alphabet size $[4, 64, 64]$ and has been optimized to have minimum rate loss under reasonable constraints and block length.

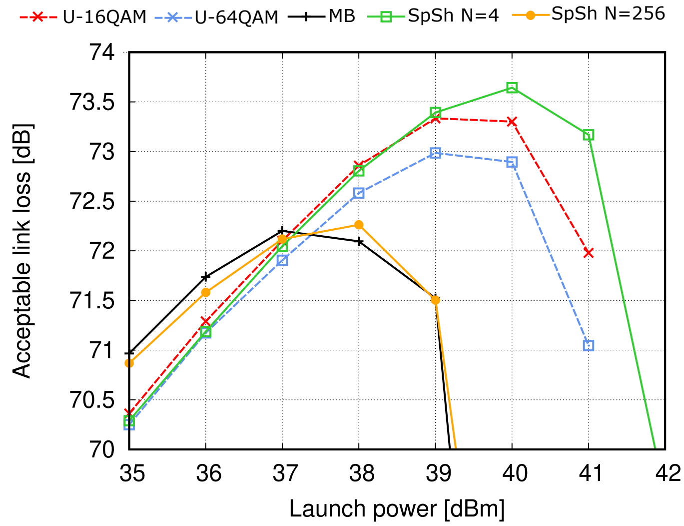

Figure 7. Performance of different uniform and shaped modulations (target GMI: 3 bits/2D; NLPC not applied).

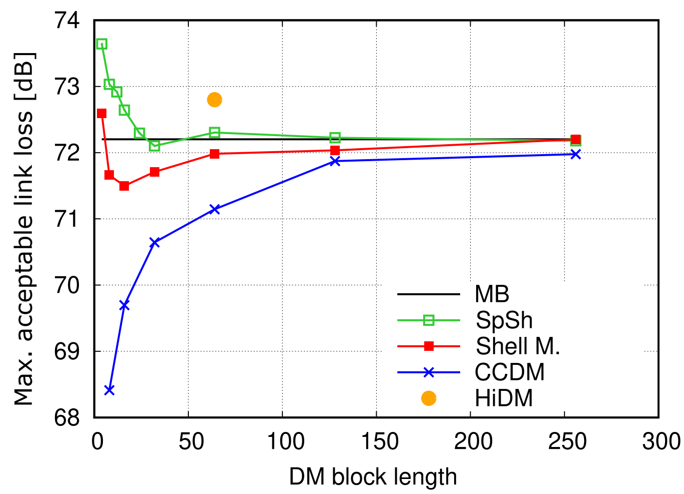

Figure 8. Performance as a function of the DM block length for different shaping strategies (target GMI: 3 bits/2D; NLPC not applied).

κ between TX and RX, on the TX and RX bandwidth, and on the oversampling factor n. Fig. 9 reports the maximum acceptable link loss as a function of the splitting ratio κ, for different bandwidth values B, with $n = 8$ and a target GMI of 3 bits/2D. As discussed in Section III-B, the effectiveness of NLPC is limited by two factors: bandwidth limitation, which acts symmetrically at the TX and RX, and signal–noise interaction, which primarily occurs at the RX. In principle, the first impairment can be mitigated by increasing the bandwidth and/or by evenly splitting the NLPC between TX and RX, whereas the second can be reduced by shifting the NLPC toward the TX. As a result, for a narrow bandwidth of $B = 55$ GHz, the optimal splitting ratio is $\kappa \approx 0.6$ (i.e., an almost even split), yielding a gain of about 3 dB relative to the baseline (without NLPC). When the bandwidth increases, only TX-side NLPC improves, whereas RX-side NLPC remains limited by signal–noise interaction. Consequently, the optimal splitting ratio shifts toward the TX, resulting in improved performance.

From a practical standpoint, however, increasing the bandwidth is generally not a viable option, as it would require allocating additional spectral resources solely to facilitate NLPC. In fact, such additional bandwidth could be exploited more efficiently by increasing the symbol rate, as shown later in this section. Therefore, larger bandwidths are considered here mainly to provide insight into the operating principles and fundamental limitations of the technique.

On the other hand, splitting NLPC between TX and RX is a viable implementation option, albeit at the cost of increased RX complexity. This aspect is particularly relevant in satellite systems, where onboard processing resources are typically constrained. Therefore, TX-side NLPC with limited bandwidth represents the simplest solution. Although suboptimal, it still provides a significant gain exceeding 2 dB.

Figure 10 shows the dependence of the performance on the oversampling factor n (bottom axis) for different NLPC configurations: TX-side NLPC ($\kappa = 1$), split NLPC with optimal splitting ($\kappa = 0.6$), and TX-side NLPC without bandwidth limitations. For each value of n, the corresponding complexity, evaluated from (13), is reported on the top axis. The figure shows that the performance of both TX-side and split NLPC saturates at $n = 2$ samples/symbol when the 55 GHz bandwidth limitation is included. In this case, the complexity of each NLPC is low, amounting to only 11 RM/2D. As expected, when DAC and ADC bandwidth limitations are removed, the performance further improves with increasing n. A similar behavior is observed for target GMIs of 3 and 5 bits/2D.

Next, Fig. 11 compares the performance of the different strategies proposed in this work, considering various shaping and NLPC configurations: (i) uniform (U) QAM constellations, (ii) constellation shaping based on PAS optimized for the nonlinear regime with $N = 4$ and LUT implementation (NL-shaping), (iii) NL shaping with TX-side NLPC, and (iv) NL shaping with NLPC split between TX and RX with $\kappa = 0.6$, all under a 55 GHz bandwidth limitation and with $n = 2$. As expected, the acceptable link loss at a GMI of 3 bits/2D is significantly higher than at 5 bits/2D—approximately 6 dB in the

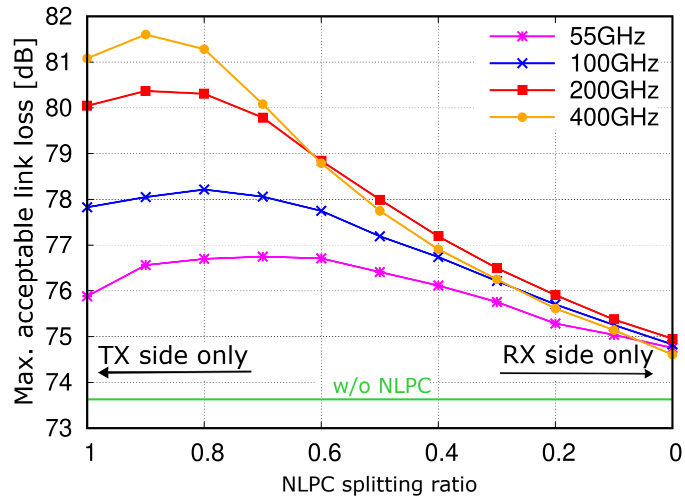

Figure 9. Performance as a function of the NLPC splitting ratio κ for different ADC/DAC bandwidths (oversampling: $n = 8$; target GMI: 3 bits/2D).

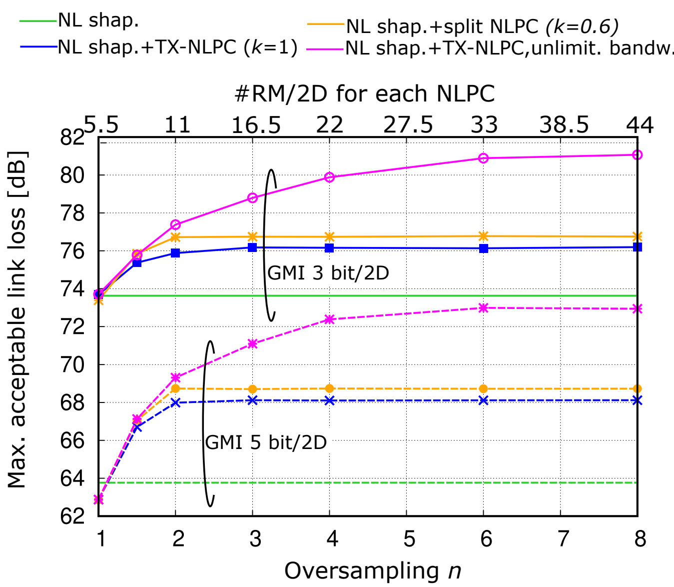

Figure 10. Performance as a function of the DSP oversampling factor n (bottom axis) and corresponding DSP complexity (top axis).

linear regime and up to 10 dB in the nonlinear regime—since a lower SNR is required. Compared to uniform constellations, NL shaping provides a gain of up to 1 dB in the nonlinear regime, while yielding approximately the same performance in the linear regime, as the conventional linear shaping gain is offset by the large rate loss due to the short block length. On top of this, NLPC provides additional improvements beyond NL shaping. In particular, TX-side NLPC yields an extra gain of more than 2 dB at a GMI of 3 bits/2D, and more than 4 dB at 5 bits/2D, relative to NL shaping alone. These gains can be further increased by about 1 dB when adopting split NLPC.

So far, assuming DAC and ADC bandwidth limitations of $B = 55$ GHz, we have considered a fixed symbol rate $R = 100$ GBd, with target GMI values of 3 bits/2D or 5 bits/2D, corresponding to overall bit rates $R_b = 2R \cdot \mathrm{GMI}$ of 600 Gb/s or 1 Tb/s, respectively. However, the same bit rates can also be

This article has been accepted for publication in Journal of Lightwave Technology. This is the author's version which has not been fully edited and
content may change prior to final publication. Citation information: DOI 10.1109/JLT.2026.3717366

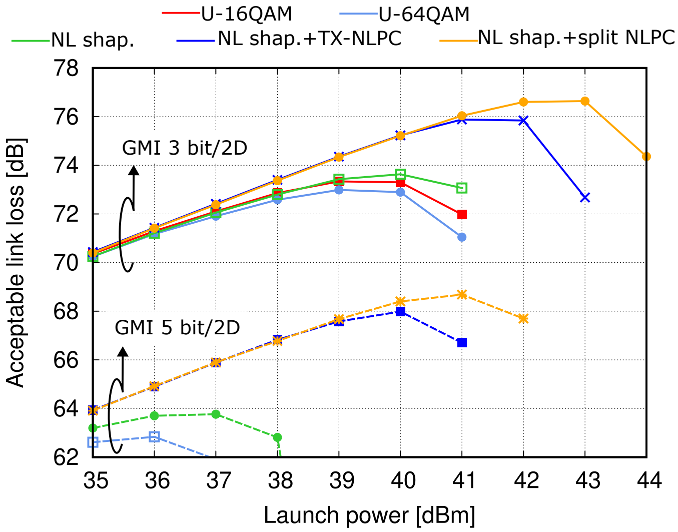

Figure 11. Performance of different DSP techniques, for target GMIs of 5 bits/2D (dashed) and 3 bits/2D (solid), with $n = 2$.

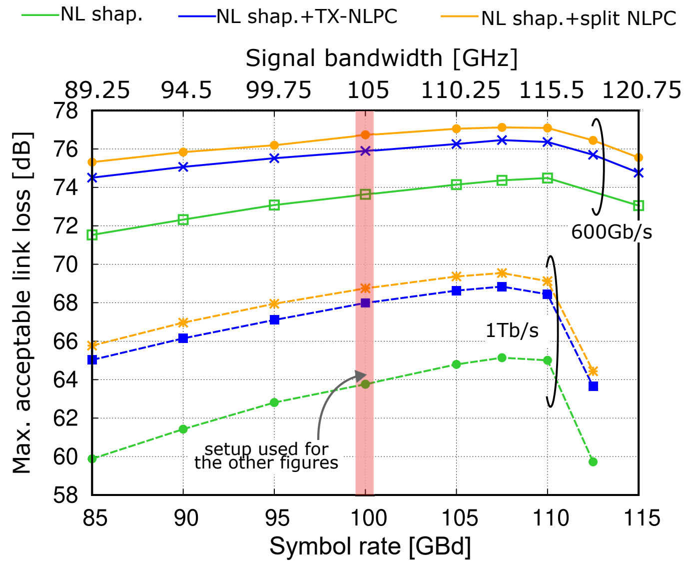

Figure 12. Performance of different DSP techniques as a function of the symbol-rate with a fixed DAC/ADC bandwidth $B = 55$ GHz and $n = 2$. The target GMI changes with the symbol rate to guarantee a fixed overall bit rate of 1 Tb/s (dashed) and 600 Gb/s (solid). The top axis reports the signal bandwidth.

achieved by varying the symbol rate R and correspondingly adapting the target GMI according to $\text{GMI} = R_b/(2R)$. Reducing R allows better containment of spectral broadening within the available bandwidth B, but requires operation at higher GMI and therefore higher SNR. Conversely, increasing R reduces the required GMI, but leaves less margin for spectral broadening and may introduce intersymbol interference even in the linear regime if the signal bandwidth exceeds B (which occurs at $R \approx 105$ GBd).

Fig. 12 evaluates this tradeoff by showing the maximum acceptable link loss as a function of the symbol rate for target data rates of (i) 600 Gb/s and (ii) 1 Tb/s. All results are obtained with $n = 2$, while varying R and selecting the target GMI accordingly.

The figure shows that the largest acceptable link loss is achieved for symbol rates slightly above 105 GBd, meaning that reducing the symbol rate to leave additional margin for spectral broadening is not advantageous. Instead, it is preferable to fully exploit the available DAC/ADC bandwidth, and even slightly exceed it, in order to operate at lower target GMI values and therefore reduce the required SNR. Although part of the signal spectrum is filtered by the finite DAC/ADC bandwidth in this regime, the benefit associated with the reduced GMI requirement more than compensates for the corresponding bandwidth penalty.

D. Performance Across Amplification Setups and Simplified-Model Validation

The objective of this section is to compare the system performance obtained with the different HPOA setups described in Section IV-A with that predicted by the simplified dispersionless model in Fig. 3, in order to assess both (i) the validity of the simplified model and (ii) the effectiveness and generality of the proposed DSP techniques across different nonlinear propagation scenarios.

Fig. 13 shows the maximum acceptable link loss versus the characteristic nonlinear power $P_{\text{NL}} = (L_{\text{eff}}\gamma)^{-1}$. As expected, according to the simplified model (shown with a solid line), the maximum acceptable link loss increases linearly with P_{NL}, since nonlinear impairments depend only on the normalized quantity P/P_{NL}. Therefore, increasing P_{NL} allows a higher launch power P and, consequently, a larger acceptable link loss.

Interestingly, all considered HPOA configurations (markers) follows the same trend predicted by the dispersionless model, confirming that their system behaviour can be effectively captured through the single parameter P_{NL}, despite their different physical implementations. In this respect, amplifiers characterized by a lower characteristic nonlinear power P_{NL} inherently achieve better performance; however, the proposed DSP techniques remain generally applicable and provide additional performance gains for each considered setup.

Overall, Fig. 13 confirms the accuracy of the simplified model in describing HPOA-based uplinks and its suitability as a design and analysis tool, while also highlighting the robustness of the proposed DSP strategies across different amplification architectures.

V. Conclusion

This work has presented a systematic analysis of coherent optical satellite uplink systems employing high-power optical amplifiers (HPOAs). To the best of our knowledge, this represents the first comprehensive investigation of nonlinear effects arising in the HPOA stage within this emerging application domain. In contrast to long-haul fiber links, dispersion in the considered scenario is negligible, and nonlinear distortions are essentially instantaneous, manifesting predominantly as self-phase modulation and spectral broadening. This fundamentally alters the interplay between nonlinearity, noise, and bandwidth limitations, leading to a distinct operating regime compared to conventional fiber systems.

This article has been accepted for publication in Journal of Lightwave Technology. This is the author's version which has not been fully edited and content may change prior to final publication. Citation information: DOI 10.1109/JLT.2026.3717366

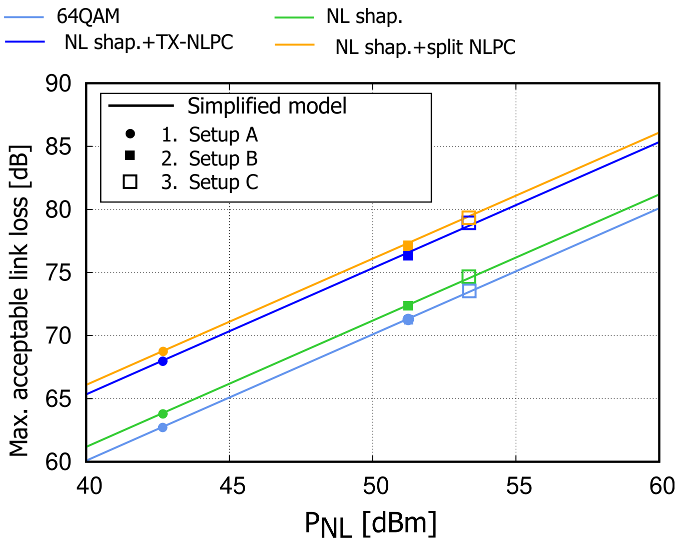

Figure 13. Performance as a function of the HPOA characteristic nonlinear power P_{NL}, for different NLPC techniques (colors). Markers correspond to specific HPOA configurations, solid lines are obtained with the simplified model. Target GMI: 5 bits/2D; oversampling: $n = 2$.

In the ideal case of unlimited bandwidth, the instantaneous nature of the nonlinear distortion enables, in principle, perfect nonlinear compensation. However, in practical systems subject to bandwidth constraints, nonlinear spectral broadening interacts with filtering and noise, making compensation more challenging. To address these limitations, DSP techniques inherited from optical fiber communications have been adapted and optimized for the satellite uplink context.

To this end, probabilistic shaping and nonlinear phase compensation (NLPC) strategies have been investigated as complementary approaches to improve system performance. Probabilistic shaping provides nonlinear tolerance and rate flexibility. Different shaping strategies have been analyzed, showing that a simple LUT-based scheme achieves the largest performance improvement with negligible complexity and minimal memory requirement, providing up to 1 dB of gain over uniform constellations. This is achieved for a very short block length, which reduces rate granularity. Adjusting the DM block length trades off rate granularity and nonlinear shaping gain, with HiDM structures offering a promising solution for further investigation. NLPC enables additional mitigation of Kerr-induced distortions with low complexity. It can be implemented at the TX, at the RX, or split between the two and requires only 11 real multiplications per 2D symbol. Overall, the combination of probabilistic shaping and split NLPC increases the acceptable link loss by about 4 dB at 600 Gb/s and 6 dB at 1 Tb/s.

The study also reveals that performance gains can be consistently achieved across a wide range of amplification configurations, despite their different physical implementations and nonlinear characteristics. Moreover, these results can be effectively interpreted through a simplified model that reduces the dependence on the detailed amplifier configuration to a single equivalent parameter. This provides a compact and accurate framework for performance prediction, enabling straightforward system assessment and comparison without requiring explicit modeling of the underlying amplifier complexity.

Future work will extend the present analysis to wavelength-division multiplexing (WDM) systems, where inter-channel nonlinear effects and spectral coexistence will introduce additional design trade-offs.

Appendix

We collect the two polarization components of the input field at times $t+\tau$ and t in the four-dimensional circularly symmetric complex Gaussian vector

$$\mathbf{z} = \begin{bmatrix} z_1 \\ z_2 \\ z_3 \\ z_4 \end{bmatrix} = \begin{bmatrix} u_x(0,t+\tau) \\ u_y(0,t+\tau) \\ u_x(0,t) \\ u_y(0,t) \end{bmatrix} \tag{14}$$

with probability distribution

$$p(\mathbf{z}) = \frac{1}{\pi^4 |\mathbf{C}|} \exp\left(-\mathbf{z}^H \mathbf{C}^{-1} \mathbf{z}\right) \tag{15}$$

where $\mathbf{C} = E\{\mathbf{z}\mathbf{z}^H\}$ is the covariance matrix and $(\cdot)^H$ denotes Hermitian conjugation. Assuming independent and statistically equivalent polarizations, $\mathbf{C}$ has a simple block structure

$$\mathbf{C} = \mathbf{C}_2 \otimes \mathbf{I}_2, \qquad \mathbf{C}_2 = \begin{bmatrix} R_0 & R_\tau \\ R_\tau^* & R_0 \end{bmatrix} \tag{16}$$

where $\mathbf{I}_m$ is the $m \times m$ identity matrix,

$$R_0 \triangleq R(0,0), \qquad R_\tau \triangleq R(0,\tau) \tag{17}$$

and $\otimes$ denotes the Kronecker product [42, Chap. 4]. The determinant and inverse of $\mathbf{C}_2$ are

$$|\mathbf{C}_2| = R_0^2 - |R_\tau|^2, \qquad \mathbf{C_2}^{-1} = \frac{1}{|\mathbf{C}_2|} \begin{bmatrix} R_0 & -R_\tau \\ -R_\tau^* & R_0 \end{bmatrix} \tag{18}$$

Letting

$$\mathbf{A} = \mathbf{A}_2 \otimes \mathbf{I}_2, \qquad \mathbf{A}_2 = \mathrm{diag}(1,-1) \tag{19}$$

the autocorrelation at distance L reads

$$\begin{aligned} R(L,t) &= E\{z_1 z_3^* \exp(-j\bar{\phi}\mathbf{z}^H \mathbf{A}\mathbf{z})\} \\ &= \frac{1}{\pi^4 |\mathbf{C}|} \int z_1 z_3^* \exp(-\mathbf{z}^\dagger \mathbf{D}\mathbf{z}) d\mathbf{z} \end{aligned} \tag{20}$$

where we have collected the terms at the exponent in a single quadratic form with matrix $\mathbf{D} = \mathbf{C}^{-1} + j\bar{\phi}\mathbf{A}$. Exploiting the block structure of $\mathbf{C}$ and $\mathbf{A}$, we rewrite $\mathbf{D} = \mathbf{D}_2 \otimes \mathbf{I}_2$, with

$$\mathbf{D}_2 = \mathbf{C}_2^{-1} + j\bar{\phi}\mathbf{A}_2 = \frac{1}{|\mathbf{C}_2|} \begin{bmatrix} R_0 + j\bar{\phi}|\mathbf{C}_2| & -R_\tau \\ -R_\tau^* & R_0 - j\bar{\phi}|\mathbf{C}_2| \end{bmatrix} \tag{21}$$

A direct computation gives

$$|\mathbf{D}_2| = \frac{1+\bar{\phi}^2 |\mathbf{C}_2|}{|\mathbf{C}_2|} \tag{22}$$

$$\mathbf{D}_2^{-1} = \frac{1}{1+\bar{\phi}^2|\mathbf{C}_2|} \begin{bmatrix} R_0 - j\bar{\phi}|\mathbf{C}_2| & R_\tau \\ R_\tau^* & R_0 + j\bar{\phi}|\mathbf{C}_2| \end{bmatrix} \tag{23}$$

Multiplying and dividing (20) by $|\mathbf{D}|$, we can interpret it as the expectation of $z_1 z_3^*$ under a Gaussian distribution with covariance matrix $\mathbf{D}^{-1}$, divided by the factor $|\mathbf{C}||\mathbf{D}|$. This expectation simply equals the corresponding term of the covariance matrix $\mathbf{D}^{-1}$, hence

$$R(L,t) = \frac{(\mathbf{D}^{-1})_{1,3}}{|\mathbf{C}||\mathbf{D}|} = \frac{(\mathbf{D}_2^{-1})_{1,2}}{|\mathbf{C}_2|^2|\mathbf{D}_2|^2} \tag{24}$$

where the second equality follows from the properties of the Kronecker product. Replacing (18) and (22)–(23) in (24), we eventually obtain

$$R(L,\tau) = \frac{R_0}{\left[1+\bar{\phi}^2(R_0^2 - |R_\tau|^2)\right]^3} \tag{25}$$

Finally, using (17) and noting that the normalization adopted in the Manakov equation (2) implies $R_0 = R(0,0) = 1/2$, we obtain the expression (8) reported in the main text.

The analysis can be extended to the M-mode version of (2)—the so called *generalized Manakov equation*, which applies for instance to the propagation in multi-mode fibers in the strong coupling regime [43]. Defining a $2M$-dimensional Gaussian vector $\mathbf{z}$ with covariance matrix $\mathbf{C} = \mathbf{C}_2 \otimes \mathbf{I}_M$ (M independent and statistical equivalent modes), and following a similar derivation (replacing $\mathbf{I}_2$ with $\mathbf{I}_M$ everywhere), one obtains

$$R(L,\tau) = \frac{R(0,\tau)}{\left[1+\bar{\phi}^2\left((1/M)^2 - |R(0,\tau)|^2\right)\right]^{M+1}} \tag{26}$$

For $M = 1$, the well-known result for the scalar nonlinear Schrödinger equation is recovered [44], [45, eq. (4.1.20)] .

Acknowledgment

This work was supported by the European Union - Next Generation EU under the Italian National Recovery and Resilience Plan (NRRP), Mission 4, Component 2, Investment 1.3, CUP J53C22003120001, CUP B53C22003970001, partnership on "Telecommunications of the Future" (PE00000001 - program "RESTART").

References

[1] H. Kaushal and G. Kaddoum, "Optical communication in space: Challenges and mitigation techniques," *IEEE communications surveys & tutorials*, vol. 19, no. 1, pp. 57–96, 2016.

[2] R. Li, B. Lin, Y. Liu, M. Dong, and S. Zhao, "A survey on laser space network: terminals, links, and architectures," *IEEE Access*, vol. 10, pp. 34815–34834, 2022.

[3] R. Boddeda, D. R. Arrieta, S. Almonacil, J. Renaudier, and S. Bigo, "Achievable capacity of geostationary-ground optical links," *Journal of Lightwave Technology*, vol. 41, no. 12, pp. 3717–3725, 2023.

[4] R. Boddeda, D. R. Arrieta, S. Bigo, S. Rabeh, S. Almonacil, A. Ghazisaeidi, E. Dutisseuil, H. Mardoyan, and J. Renaudier, "Current state, prospects, and opportunities for reaching beyond 100 Gbps per carrier using coherent optics in satellite communications," in *ECOC 2024; 50th European Conference on Optical Communication*, pp. 406–409, VDE, 2024.

[5] R. Barrios, S. Dimitrov, R. Mata-Calvo, and D. Giggenbach, "Link budget assessment for GEO feeder links based on optical technology," *International Journal of Satellite Communications and Networking*, vol. 39, no. 2, pp. 160–177, 2021.

[6] D. Giggenbach and A. Shrestha, "Atmospheric absorption and scattering impact on optical satellite-ground links," *International Journal of Satellite Communications and Networking*, vol. 40, no. 2, pp. 157–176, 2022.

[7] N. K. Lyras, C. I. Kourogiorgas, and A. D. Panagopoulos, "Cloud free line of sight prediction modeling for low earth orbit optical satellite networks," in *International Conference on Space Optics ICSO 2018*, vol. 11180, pp. 555–563, SPIE, 2019.

[8] L. C. Roberts Jr, S. R. Meeker, J. Tesch, J. C. Shelton, J. E. Roberts, S. F. Fregoso, T. Troung, M. Peng, K. Matthews, H. Herzog, *et al.*, "Performance of the adaptive optics system for laser communications relay demonstration's ground station 1," *Applied Optics*, vol. 62, no. 23, pp. G26–G36, 2023.

[9] I. Dror, A. Sandrov, and N. S. Kopeika, "Experimental investigation of the influence of the relative position of the scattering layer on image quality: the shower curtain effect," *Applied optics*, vol. 37, no. 27, pp. 6495–6499, 1998.

[10] D. Aviv, *Laser space communications*. Artech, 2006.

[11] L. V. Kotov, V. Temyanko, M. M. Bubnov, D. S. Lipatov, A. S. Lobanov, A. Abramov, S. S. Aleshkina, A. N. Guryanov, and M. E. Likhachev, "High-energy single-frequency core-pumped Er-doped fiber amplifiers," *Journal of Lightwave Technology*, vol. 41, no. 5, pp. 1526–1532, 2022.

[12] L. V. Kotov, M. E. Likhachev, M. M. Bubnov, O. I. Medvedkov, M. V. Yashkov, A. N. Guryanov, S. Février, J. Lhermite, and E. Cormier, "Yb-free Er-doped all-fiber amplifier cladding-pumped at 976 nm with output power in excess of 100 W," in *Fiber Lasers XI: Technology, Systems, and Applications*, vol. 8961, pp. 149–154, SPIE, 2014.

[13] T. Matniyaz, F. Kong, M. T. Kalichevsky-Dong, and L. Dong, "302 W single-mode power from an Er/Yb fiber MOPA," *Optics Letters*, vol. 45, no. 10, pp. 2910–2913, 2020.

[14] J. W. Nicholson, A. Grimes, B. Zhu, C. Jin, V. S. Sudarshanam, A. Hariharan, and D. J. DiGiovanni, "High-power fiber lasers for free-space optical communication uplinks," *IEEE Journal of Selected Topics in Quantum Electronics*, 2025.

[15] K. G. Petrillo, J. Cook, D. Engin, A. Sincore, and A. M. Schober, "Optical fiber amplifiers for satellite communications," *IEEE Journal of Selected Topics in Quantum Electronics*, vol. 32, no. 1: Advances in Free Space Laser Communications, pp. 1–13, 2026.

[16] S. Lévêque, A. Maho, L. Bramerie, M. Gay, M. Sotom, M. Joindot, and T. Chartier, "Assessing nonlinear effects in high-power optical amplifiers for WDM FSO communications up to 200 Gbps per channel," in *2025 IEEE International Conference on Space Optical Systems and Applications (ICSOS)*, pp. 1–8, 2025.

[17] V. Billault, S. Leveque, A. Maho, M. Welch, J. Bourderionnet, E. Lallier, M. Sotom, A. L. Kernec, and A. Brignon, "Optical coherent combining of high-power optical amplifiers for free-space optical communications," *Optics Letters*, vol. 48, no. 14, pp. 3649–3652, 2023.

[18] E. Ciaramella and G. Cossu, "Nonlinear fiber effects in ultra-high power 10×10 Gbit/s WDM-IM free-space systems for satellite links," *Optics Express*, vol. 32, no. 5, pp. 7959–7968, 2024.

[19] A. Grimes, B. Zhu, C. Jin, and J. W. Nicholson, "10 Gbps transmission from a high power EDFA for free space communications," in *2024 IEEE Photonics Society Summer Topicals Meeting Series (SUM)*, pp. 1–4, IEEE, 2024.

[20] F. P. Guiomar, M. A. Fernandes, J. L. Nascimento, V. Rodrigues, and P. P. Monteiro, "Coherent free-space optical communications: Opportunities and challenges," *Journal of Lightwave Technology*, vol. 40, no. 10, pp. 3173–3186, 2022.

[21] Keopsys by Lumibird, "Fiber amplifier – High power multi stages EDFA." https://www.keopsys.com/portfolio/fiber-amplifier-c-pb-hp-series/, 2026. Accessed: 2026-05-07.

[22] S. Civelli, M. Secondini, and L. Potì, "Nonlinearity mitigation for coherent ground-to-satellite optical links," *arXiv preprint arXiv:2601.05655*, 2026.

[23] C. R. Menyuk and B. S. Marks, "Interaction of polarization mode dispersion and nonlinearity in optical fiber transmission systems," vol. 24, no. 7, p. 2806, 2006.

[24] G. P. Agrawal, *Nonlinear fiber optics*. Academic Press, 2001.

[25] S. Civelli, E. Forestieri, and M. Secondini, "On the nonlinear shaping gain with probabilistic shaping and carrier phase recovery," *Journal of Lightwave Technology*, vol. 10, no. 41, pp. 3046–3056, 2022.

[26] G. Böcherer, F. Steiner, and P. Schulte, "Bandwidth efficient and rate-matched low-density parity-check coded modulation," *IEEE Transactions on Communications*, vol. 63, no. 12, pp. 4651–4665, 2015.

[27] P. Schulte and G. Böcherer, "Constant composition distribution matching," *IEEE Transactions on Information Theory*, vol. 62, no. 1, pp. 430–434, 2016.

[28] Y. Gültekin, W. van Houtum, and F. Willems, "On constellation shaping for short block lengths," in *2018 Symposium on Information Theory and Signal Processing in the Benelux (SITB 2018)*, pp. 86–96, University of Twente, 2018.

[29] T. Yoshida, M. Karlsson, and E. Agrell, "Hierarchical distribution matching for probabilistically shaped coded modulation," *Journal of Lightwave Technology*, vol. 37, no. 6, pp. 1579–1589, 2019.

[30] S. Civelli and M. Secondini, "Hierarchical distribution matching for probabilistic amplitude shaping," *Entropy*, vol. 22, no. 9, p. 958, 2020.

[31] F. Buchali, F. Steiner, G. Böcherer, L. Schmalen, P. Schulte, and W. Idler, "Rate adaptation and reach increase by probabilistically shaped 64-QAM: An experimental demonstration," *Journal of Lightwave Technology*, vol. 34, no. 7, pp. 1599–1609, 2016.

[32] T. Fehenberger, A. Alvarado, G. Böcherer, and N. Hanik, "On probabilistic shaping of quadrature amplitude modulation for the nonlinear fiber channel," *Journal of Lightwave Technology*, vol. 34, no. 21, pp. 5063–5073, 2016.

[33] S. Civelli, E. Forestieri, and M. Secondini, "Sequence-selection-based constellation shaping for nonlinear channels," *Journal of Lightwave Technology*, vol. 42, no. 3, pp. 1031–1043, 2024.

[34] A. Wenzler and E. Luder, "New structures for complex multipliers and their noise analysis," in *1995 IEEE International Symposium on Circuits and Systems (ISCAS)*, vol. 2, pp. 1432–1435, IEEE, 1995.

[35] A. Alvarado, T. Fehenberger, B. Chen, and F. M. Willems, "Achievable information rates for fiber optics: Applications and computations," *Journal of Lightwave Technology*, vol. 36, no. 2, pp. 424–439, 2018.

[36] T. Fehenberger, D. S. Millar, T. Koike-Akino, K. Kojima, and K. Parsons, "Multiset-partition distribution matching," *IEEE Transactions on Communications*, vol. 67, no. 3, pp. 1885–1893, 2018.

[37] T. Pfau, S. Hoffmann, and R. Noé, "Hardware-efficient coherent digital receiver concept with feedforward carrier recovery for M-QAM constellations," *Journal of Lightwave Technology*, vol. 27, no. 8, pp. 989–999, 2009.

[38] J. Cho, L. Schmalen, and P. J. Winzer, "Normalized generalized mutual information as a forward error correction threshold for probabilistically shaped QAM," in *2017 European Conference on Optical Communication (ECOC)*, pp. 1–3, IEEE, 2017.

[39] T. Fehenberger, D. S. Millar, T. Koike-Akino, K. Kojima, K. Parsons, and H. Griesser, "Analysis of nonlinear fiber interactions for finite-length constant-composition sequences," *Journal of Lightwave Technology*, vol. 38, no. 2, pp. 457–465, 2020.

[40] T. Fehenberger, H. Griesser, and J.-P. Elbers, "Mitigating fiber nonlinearities by short-length probabilistic shaping," in *Optical Fiber Communication Conference*, pp. Th1I–2, Optical Society of America, 2020.

[41] K. Wu, G. Liga, M. Secondini, and A. Alvarado, "Accounting for temporal energy correlations in the enhanced Gaussian noise model," in *2025 Optical Fiber Communications Conference and Exhibition (OFC)*, pp. 1–3, IEEE, 2025.

[42] R. A. Horn and C. R. Johnson, *Topics in Matrix Analysis*. Cambridge University Press, 1991.

[43] A. Mecozzi, C. Antonelli, and M. Shtaif, "Nonlinear propagation in multi-mode fibers in the strong coupling regime," *Optics express*, vol. 20, no. 11, pp. 11673–11678, 2012.

[44] J. T. Manassah, "Self-phase modulation of incoherent light revisited," *Optics letters*, vol. 16, no. 21, pp. 1638–1640, 1991.

[45] G. P. Agrawal, *Fiber-optic communication systems*. John Wiley & Sons, 2012.